Effects of quantum interferences among crystal-momentum-resolved electrons in solid high-order harmonic generation

Xi Liu,[1,4,*] Yujie Li,[1] Dongdong Liu,[1,4] Xiaosong Zhu,[2,†] Xiaofan Zhang,[3] and Peixiang Lu[2,3]

[1]*School of Physics and New Energy, Xuzhou University of Technology, Xuzhou 221018, China*

[2]*School of Physics and Wuhan National Laboratory for Optoelectronics, Huazhong University of Science and Technology, Wuhan 430074, China*

[3]*Hubei Key Laboratory of Optical Information and Pattern Recognition, Wuhan Institute of Technology, Wuhan 430205, China*

[4]*State Key Laboratory of Millimeter Waves, Southeast University, Nanjing 210096, China*

(Received 14 October 2020; accepted 17 February 2021; published 5 March 2021)

We theoretically demonstrate the effects of quantum interferences among valence electrons with various initial crystal momenta in the high-order harmonic generation (HHG) in solids. By investigating crystal-momentum-dependent harmonics from solids in linearly polarized laser fields, some unique radiation characteristics of the observed overall harmonics are attributed to the consequences of interferences among valence electrons with different crystal momenta. It is shown that the electron pairs with opposite crystal momenta result in the destructive interferences of even-order harmonics for a crystal with the inversion symmetry, which eventually leads to the only odd orders in observed overall harmonic spectra for a semiconductor material because of the complete pairing of all valence electrons. Additionally, each of the harmonic plateaus in the overall multiple-plateau harmonic spectrum is identified to be contributed by the valence electrons within different crystal momentum zones. We also find that the solid-phase HHG in the below-band-gap region is substantially suppressed due to the collective responses of multiple valence electrons. This work sheds light on the essential impacts of interferences among crystal-momentum-resolved electrons on the HHG in solids and is helpful to explore ultrafast coherent processes in condensed matter.

DOI: 10.1103/PhysRevA.103.033104

I. INTRODUCTION

High-order harmonic generation (HHG) [1–5] is one of the most attractive phenomena induced by the interaction of intense laser fields with atomic and molecular gases. As a highly nonlinear optical radiation, HHG is widely recognized as a promising route to generate coherent attosecond extreme ultraviolet (EUV) and soft x-ray laser pulses [6,7]. The recent experimental observations of HHG from several crystalline solids [8–10] have extended the target media from gases to condensed-matter systems. The high conversion efficiency and low driving laser intensity of solid-phase HHG make it a potential tool to obtain high-efficiency and compact attosecond light sources. The information of electronic states and crystallographic structures of solid targets can be decoded using the high harmonic signals. High harmonic spectroscopy in solids offers an opportunity to reconstruct the energy-band structures [11,12], probe crystalline symmetries [13–16], measure Berry curvatures [17,18], and even to detect topological phase transitions (TPTs) [19–21]. The solid-phase HHG opens up a new field of studying attosecond electron dynamics in condensed materials [22–26].

The periodicity and complexity of solid systems give rise to some particular properties of solid-phase harmonic radiations [27,28]. Compared with gas-phase HHG, the motions of laser-driven electrons in the solid-phase HHG processes are highly delocalized over the crystal lattice. Hence the physical mechanisms and radiation characteristics of the solid-phase HHG are distinctively different from those of the harmonics generated from atoms and molecules [29,30]. For instance, theoretical [31,32] and experimental [33] studies have shown that the high harmonic spectra from solids exhibit multiple-plateau structures due to the electronic transitions from multiple conduction bands to valance bands. It is widely recognized that HHG in solids is contributed by two major mechanisms: laser-induced intraband Bloch oscillations and interband dipole transitions. The generated harmonics from the two mechanisms differ significantly in many respects. For example, it has emerged that the intraband and interband HHG display fundamental different wavelength dependencies in the harmonic yield and cutoff energy [34,35]. The intraband and interband HHG dominate the observed harmonic spectrum in the below-band-gap region and harmonic plateau, respectively, for a midinfrared (MIR) laser pulse [31].

In many studies, the light-matter interactions in solids are described by a single active election (SAE) model [31,36–39]. In this model, the solid-phase HHG is attributed to the laser-induced response of a single valence electron with a specific crystal momentum (such as the Γ point) in the valence band. The neglect of the electrons with other crystal momenta is effective under certain conditions. Thus the SAE model in solids provides valuable insights into the HHG process in

*liuxi@xzit.edu.cn

†zhuxiaosong@hust.edu.cn

many aspects. However, ultimately, the HHG response in solids is essentially an ultrafast dynamics involving all valence electrons with multiple crystal momenta. Some recent works [40–45] have reported that the contributions from the electrons with different crystal momenta in valence bands play an important role for the HHG in solids. For instance, Lü *et al.* [42] have found an abnormal yield dependence of the intraband HHG on the laser intensity due to the coherence of harmonics emitted from multiple valence electrons. The collective excitations of valence electrons and the interferences among multiple valence electrons in solid-phase HHG have attracted increasing attention in the strong-field research field.

In this work, we investigate the effects of quantum interferences among multiple valence electrons in the HHG from a band-gap semiconductor. By solving the time-dependent Schrödinger equation (TDSE) with a series of initial crystal momenta, some particular features of observed overall harmonics are found to stem from the interferences among the valence electrons with various crystal momenta. The involved radiation characteristics are mainly focused on the selection rules of the HHG, multiple plateaus of the harmonic spectra, and the yields of below-band-gap harmonics. Specifically, for a crystal with inversion symmetry in a linearly polarized (LP) laser field, the absences of even-order harmonics are attributed to the destructive interferences between the electron pairs with opposite crystal momenta. The multiple plateaus of overall harmonics are contributed by the valence electrons within different crystal momentum regions. The valence electrons with crystal momenta farther away from the Γ point dominate the higher harmonic plateaus and the corresponding cutoff energies in the overall harmonic spectra. The contributions of multiple valence electrons with various crystal momenta also result in the significant suppression of below-band-gap harmonics. Our studies illustrate the crucial influence of field-induced electron dynamics involving multiple crystal momenta on solid-phase HHG and deepen our understanding of ultrafast electron dynamics in solids.

This paper is organized as follows. In Sec. II we describe the adopted theoretical model in this work and present the numerical method in our simulations. In Sec. III we investigate the selection rules of observed harmonics for a crystal with inversion symmetry in a LP laser field and clarify the fact that the disappearance of even-order harmonics is due to the destructive interference between the electron pairs with opposite crystal momenta. In Sec. IV we discuss the contributions of valence electrons with different crystal momenta to the observed overall harmonic plateaus and the corresponding cutoff energies. In Sec. V a remarkable reduction of harmonic yields in the below-band-gap region is studied. We summarize our work in Sec. VI.

II. THEORETICAL MODEL

In our simulations the crystal target is mimicked by a one-dimensional band-gap semiconductor model. The laser field is polarized along the crystal axis. The electron dynamics induced by laser-crystal interactions are described by the one-dimensional TDSE within the independent-electron approximation. The valence bands are initially occupied by the electrons with various crystal momenta. For the electron initially lying in band n with an initial crystal momentum k, the TDSE in the velocity gauge is written as (atomic units are used throughout this paper unless otherwise stated)

$$i\frac{\partial}{\partial t}\psi_{nk}(x,t)=\left\{\frac{[\hat{p}+A(t)]^2}{2}+V(x)\right\}\psi_{nk}(x,t), \tag{1}$$

where $\psi_{nk}(x,t)$ is the time-dependent wave function, $\hat{p}$ is the momentum operator, and $A(t)$ is the vector potential of the laser field. $V(x)$ is the periodic lattice potential with lattice constant a_0, i.e., $V(x)=V(x+a_0)$. Herein, we use the Gaussian-type potential [37,46]

$$V(x)=-V_0e^{-\frac{x^2}{\alpha}} \tag{2}$$

in the unit-cell region of $x\in[-a_0/2,a_0/2]$ with $V_0=1.6$ a.u. and $\alpha=1.2$ a.u. The lattice constant is chosen as $a_0=6$ a.u. The dipole approximation is employed because the adopted wavelengths in our simulations are much larger than the lattice constant.

According to Bloch's theorem, $\psi_{nk}(x,t)$ can be decomposed in the form of

$$\psi_{nk}(x,t)=e^{ikx}u_{nk}(x,t), \tag{3}$$

where the wave function $u_{nk}(x,t)$ is periodic with the same periodicity as the crystal lattice, i.e., $u_{nk}(x,t)=u_{nk}(x+a_0,t)$. By substituting Eq. (3) into Eq. (1), we obtain the motion equation of wave function $u_{nk}(x,t)$ as

$$i\frac{\partial}{\partial t}u_{nk}(x,t)=\hat{H}_k(t)u_{nk}(x,t), \tag{4}$$

where $\hat{H}_k$ is a k-dependent Hamiltonian and is expressed as

$$\hat{H}_k(t)=\frac{[\hat{p}+k+A(t)]^2}{2}+V(x). \tag{5}$$

Consequently, the dynamics of electrons in laser fields can be completely depicted with the periodic wave function $u_{nk}(x,t)$ under k-dependent $\hat{H}_k$. Because the crystal momentum k and vector potential $A(t)$ are independent of coordinate variables x, $\hat{H}_k$ still retains the lattice periodicity. Considering the periodicity of $u_{nk}(x,t)$, Eq. (4) can be solved only in the unit-cell zone of $x\in[-a_0/2,a_0/2]$ with the periodic boundary condition (PBC). Since the crystal momentum k is always a good quantum number, Eq. (4) can be solved independently for each k.

We numerically solve Eq. (4) by using the spectral method with plane-wave bases. Specifically, the time-dependent wave function $u_{nk}(x,t)$ is expanded as

$$u_{nk}(x,t)=\sum_{m=-N_b}^{m=N_b}c_{nk}^m(t)q_m(x) \tag{6}$$

in the unit-cell zone $x\in[-a_0/2,a_0/2]$ using $2N_b+1$ basis functions, where $c_{nk}^m(t)$ is the time-dependent expansion coefficient. In Eq. (6), $q_m(x)$ is the expression of the plane-wave basis and is written as

$$q_m(x)=\frac{1}{\sqrt{a_0}}\exp\left(i\frac{2\pi mx}{a_0}\right), \tag{7}$$

where m is an integer representing the basis index. Hence, the k-dependent Hamiltonian operator $\hat{H}_k$ can be represented

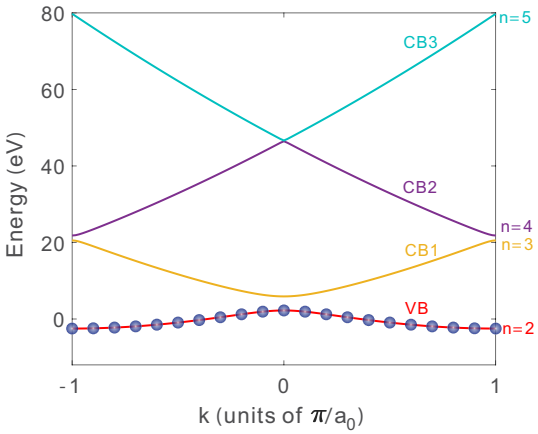

FIG. 1. Band structures of the highest valence band VB ($n = 2$) and first three conduction bands CB1, CB2, and CB3 ($n = 3, 4, 5$). The lowest valence band VB0 ($n = 1$) is not shown. The valence band VB is fully occupied with electrons initially for a band-gap semiconductor.

by a $(2N_b + 1)$-order square matrix $\mathbf{H}_k$. $\mathbf{H}_k$ is calculated as $\mathbf{H}_k(t) = [\mathbf{p} + k + A(t)]^2/2 + \mathbf{V}$. $\mathbf{p}$ is the momentum matrix with the matrix element $\mathbf{p}_{m'm} = \langle q_{m'}(x)|\hat{p}|q_m(x)\rangle = \frac{2m\pi}{a_0}\delta_{m'm}$. $\mathbf{V}$ is the potential matrix with the matrix element $\mathbf{V}_{m'm} = \langle q_{m'}(x)|V(x)|q_m(x)\rangle$. Thus Eq. (4) can be solved with the matrix form

$$i\frac{\partial}{\partial t}\mathbf{C}_{nk}(t) = \mathbf{H}_k(t)\mathbf{C}_{nk}(t), \tag{8}$$

where $\mathbf{C}_{nk}(t)$ is a column matrix composed of a sequence of coefficients $c^m_{nk}(t)$.

The energy-band structures and time-independent wave functions of the crystals are obtained by solving the eigenvalue equation of the field-free Hamiltonian matrix $\mathbf{H}_{0,k}$. $\mathbf{H}_{0,k}$ is calculated as $\mathbf{H}_{0,k} = (\mathbf{p} + k)^2/2 + \mathbf{V}$. Figure 1 shows the calculated energy-band structures using the diagonalization method. One can see clearly that four bands ($n = 2, 3, 4, 5$) are presented and are denoted as VB, CB1, CB2, and CB3, respectively. The minimum band-gap energy between the valence band VB and the first conduction band CB1 at the Γ point (i.e., $k = 0$) is $E_g = 3.67$ eV. Since the lowest valence band VB0 ($n = 1$) is extremely flat and deeply bound, the HHG responses involving the electrons in VB0 are negligible. Thus our model only focuses on the valence band VB ($n = 2$) and ignores the contributions from valence band VB0. As a band-gap semiconductor, the valence band VB is initially fully occupied across the whole Brillouin zone (BZ) by the crystal-momentum-resolved electrons as shown in Fig. 1.

Equation (8) is propagated using the Crank-Nicolson (CN) algorithm [47]

$$\mathbf{C}_{nk}(t + \Delta t) = \frac{1 - i\frac{\Delta t}{2}\mathbf{H}_k\left(t + \frac{\Delta t}{2}\right)}{1 + i\frac{\Delta t}{2}\mathbf{H}_k\left(t + \frac{\Delta t}{2}\right)}\mathbf{C}_{nk}(t). \tag{9}$$

In our simulations, the time step is chosen as $\Delta t = 0.02$ a.u. The laser wavelength adopted in our all calculations is 3200 nm. The laser intensity is 4×10^{11} W/cm^2 for all calculations unless otherwise stated. The total duration of the laser pulse is eight optical cycles. We adopt the sine-squared envelope for all laser pulses except those used in Sec. III. The basis parameter N_b is adopted as 100. The laser-induced current from the valence electron initially lying in the given band n with crystal momentum k is calculated as [44]

$$j_{nk}(t) = \langle u_{nk}|\hat{p} + k + A(t)|u_{nk}\rangle = \mathbf{C}^{\dagger}_{nk}[\mathbf{p} + k + A(t)]\mathbf{C}_{nk}. \tag{10}$$

The observed overall harmonic spectrum is the coherent superposition of the harmonics emitted by all electrons in the valence bands. Hence the total current is calculated by summing j_{nk} over the band indices n and crystal momenta k as

$$j_{\text{total}}(t) = \frac{1}{N_k a_0}\sum_{nk} j_{nk}(t), \tag{11}$$

where N_k is the number of BZ sample points. We adopt the equally spaced k meshes in the reduced BZ $[-\pi/a_0, \pi/a_0]$. The crystal momentum step is fixed as $2\pi/(a_0 N_k)$, where N_k is chosen as 121. The high harmonic spectra are obtained by the Fourier transform of the corresponding laser-induced current. A Hanning window [32,36] is used to improve the signal-to-noise ratio before applying the Fourier transformation. It should be noted that our model cannot cover the electron correlation effects and only includes the interference effects of independent multiple valence electrons in solid-phase HHG. Many studies [48–50] have reported that the Coulomb interactions between electrons have a very weak effect on the HHG in the general solids and therefore can be neglected.

III. SELECTION RULES OF HHG

The selection rule of the high harmonic spectrum is a fundamental issue of common concern in the field of strong-field physics. In gas-phase HHG, the selection rule is completely determined by the invariance of the full time-dependent Hamiltonian under an N-fold dynamical symmetry transformation [51,52]. Based on this, the allowed harmonic orders in the gas-phase harmonic spectrum can be intuitively judged by the associated rotational symmetry (ARS) of the atomic or molecular target and the driving laser field [53–55]. Likewise, the selection rule of the solid-phase HHG has attracted extensive attention and is also revealed to be determined by the dynamical symmetry of the laser-matter system in some recent works [14,56–58]. Just as the case of gas-phase HHG, when a crystal with inversion symmetry is irradiated by a monochromatic LP laser field, only odd-order harmonics can be observed [8,59]. By investigating the allowed orders of the solid-phase harmonic spectra from the valence electrons with various crystal momenta, we confirm that the suppression of even-order harmonics is caused by the destructive interferences between harmonics emitted from valence electron pairs with opposite crystal momenta for a crystal with inversion symmetry in a LP laser field. Considering that the electrons initially fully occupy the whole BZ in valence bands, the complete paired matching of all valence electrons results in the disappearances of even orders in the observed overall harmonic spectra.

We first investigate the situation that the valence electrons are located at neither Γ point nor Bragg plane, i.e., $k \neq 0$ and $k \neq \pm\pi/a_0$. The selection rules of high harmonic spectra from the valence electrons at high-symmetry points

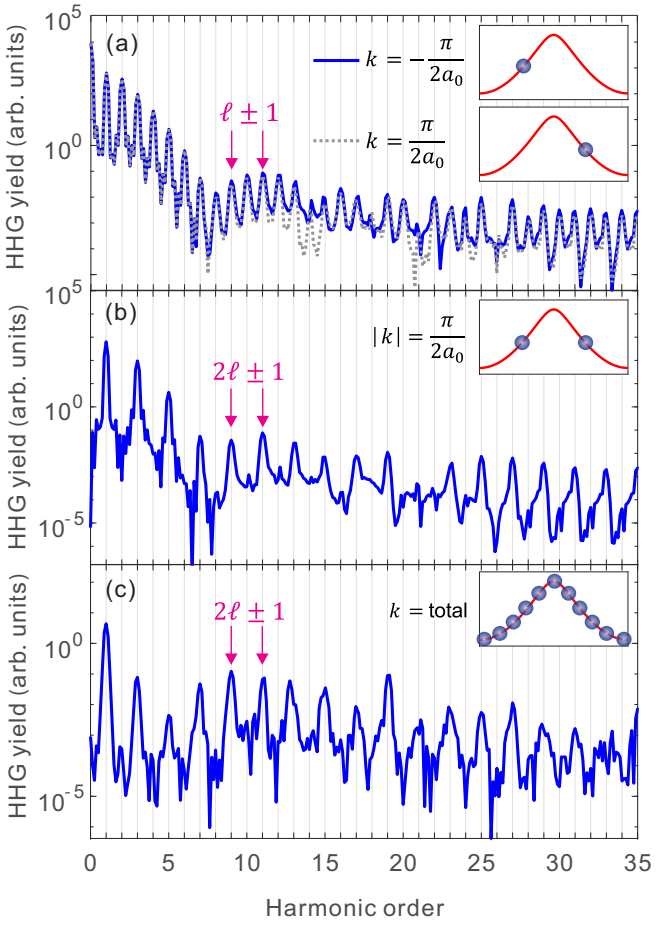

FIG. 2. High harmonic spectra contributed by valence electrons with various crystal momenta: (a) $k = \pm\pi/(2a_0)$, (b) $|k| = \pi/(2a_0)$, and (c) $k \in [-\pi/a_0, \pi/a_0]$.

will be discussed in detail later. The valence electrons with crystal momenta $k = \pm\pi/(2a_0)$ are chosen as the examples. Figure 2(a) shows the calculated harmonic spectra from the valence electrons with $k = -\pi/(2a_0)$ and $k = \pi/(2a_0)$. In order to obtain clear and sharp radiation peaks in the harmonic spectra, we adopt a trapezoidal laser envelope with a total duration of eight optical cycles (two-cycle linear ramps and four-cycle constant centers) for all laser pulses in this section. As shown in Fig. 2(a), the harmonics emitted from these two valence electrons highly coincide with each other. More importantly, both of these two harmonic spectra contain both odd and even orders. We further investigate the selection rule of the total harmonic spectrum from these two electrons with opposite crystal momenta. Figure 2(b) shows the obtained harmonic spectrum by considering two electrons with $k = \pm\pi/(2a_0)$. One can see clearly that only odd-order harmonics appear in the synthetic harmonic spectrum. As mentioned above, the even-order harmonics can be observed for an individual valence electron with $k = -\pi/(2a_0)$ or $k = \pi/(2a_0)$. Hence the destructive interferences between the electrons with $k = -\pi/(2a_0)$ and $k = \pi/(2a_0)$ result in the disappearances of even-order harmonics in the synthetic harmonic spectrum.

Similarly to the gas-phase HHG, the allowed harmonic orders can be interpreted by the inversion symmetry of k-dependent free-field Hamiltonian

$$\hat{H}_{0,k} = \frac{(\hat{p}+k)^2}{2} + V(x). \tag{12}$$

Specifically, considering the inversion symmetry of the crystal, i.e., $V(-x) = V(x)$, $\hat{H}_{0,k}$ becomes $\hat{H}_{0,-k}$ under the inversion transformation $\hat{\mathcal{P}} = (x \to -x)$, i.e., $\hat{\mathcal{P}}\hat{H}_{0,k} = \hat{H}_{0,-k}$. Accordingly, the inversion operator $\hat{\mathcal{P}}$ turns the periodic wave function $u_k(x)$ into $u_{-k}(x)$. These results indicate that the inversion symmetries of the systems composed of two electrons with opposite crystal momenta should be treated in pairs as in Ref. [60]. The two electrons with opposite crystal momenta are the inversion symmetric partners to each other. The paired symmetric partners permit the inversion symmetries of the systems because of $\hat{\mathcal{P}}(\hat{H}_{0,k}, \hat{H}_{0,-k}) = (\hat{H}_{0,k}, \hat{H}_{0,-k})$. The inversion symmetries of paired inversion symmetric partners lead to the vanishing even-order components of the synthetic currents contributed by corresponding valence electrons. This is the reason why the even harmonics disappear for two electrons with opposite crystal momenta as shown in Fig. 2(b). When only a single valence electron ($k \neq 0$ and $k \neq \pm\pi/a_0$) is considered, the unpaired symmetric partner results in the broken inversion symmetry of the system. Thus even harmonics appear as shown in Fig. 2(a). The observed overall harmonics are contributed by all electrons in valence bands. Because the electrons initially fully occupy the whole BZ, all valence electrons with positive and negative crystal momenta can be completely matched in pairs. Thus only odd-order harmonics are observed in the overall harmonic spectrum. Figure 2(c) shows the calculated harmonic spectrum contributed by all valence electrons with $k \in [-\pi/a_0, \pi/a_0]$ in the VB. One can see that only odd-order harmonics emerge in the overall harmonic spectrum. This result is in good accordance with our conclusion. Owing to the pair matching between two electrons with opposite crystal momenta in sign, the total contribution from the electron pair with $-k$ and k is denoted as $|k|$ in this paper.

We then investigate the selection rules of high harmonic spectra from valence electrons at high-symmetry points, i.e., $k = 0$ or $k = \pm\pi/a_0$. It is noted that the electron at the high-symmetry point is its own inversion symmetric partner. Thus, the inversion symmetry of the system is preserved for a single electron at the high-symmetry point, which results in that only odd-order harmonics are observed. Figures 3(a) and 3(b) show the obtained harmonic spectra from the electrons at the Γ point $k = 0$ and Bragg plane $k = \pm\pi/a_0$, respectively. One can see that both of these harmonic spectra exhibit only odd-order harmonics. These results agree well with our conclusions. The allowed orders of the harmonic spectra contributed by the valence electrons at high-symmetry points are consistent with those of the overall harmonic spectra, which is the reason why the Γ-point-only SAE model can accurately reproduce the pure odd orders of the observed harmonic spectrum in previous studies. Our results further verify that the selection rules of solid-phase HHG stem from the symmetries of the laser-matter systems.

IV. HARMONIC PLATEAUS AND CUTOFFS

The emergence of the multiple plateaus is a unique characteristic of the harmonic spectrum in solids. The

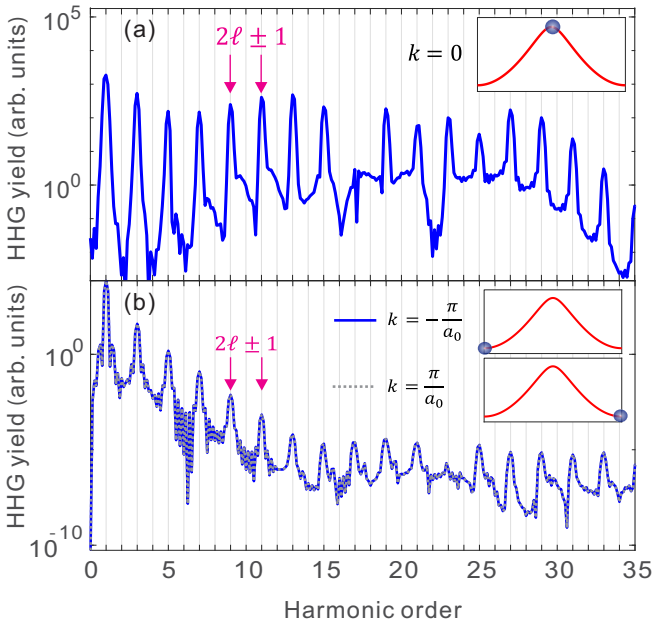

FIG. 3. High harmonic spectra contributed by the valence electrons at high-symmetry points: (a) Γ point $k = 0$, (b) Bragg plane $k = \pm\pi/a_0$.

multiple-plateau harmonic spectra stems from the electron transitions from the multiple conduction bands to valence bands in solids. The solid-phase HHG in harmonics plateaus can be described by the k-space semiclassical picture [27,31,34,39,44]. For completeness, we first revisit the k-space semiclassical picture for the multiple independent electrons as introduced in Ref. [44]. The first two harmonic plateaus are considered in our model.

As shown in Fig. 4(a), for the given electron pair with arbitrary $|k_0|$ (for the sake of simplicity, $k_0 \geqslant 0$) in the VB, the laser-driven electrons are first accelerated to Γ point (as indicated by the dashed cyan arrow) and further tunnel into CB1 (as indicated by the solid cyan arrow). Then the laser-driven electrons oscillate periodically in CB1 under the external laser field and further tunnel into CB2 when the instantaneous band gap between CB2 and CB1 reaches a minimum. Simultaneously, the occurrences of vertical transitions of laser-driven electrons from CB1 and CB2 to VB are responsible for the first and second harmonic plateaus in the harmonic spectrum, respectively. The laser-driven electrons in CB1 and CB2 satisfy the semiclassical motion equation

$$k(t) = k(0) + A(t), \tag{13}$$

where $k(t)$ is the instantaneous crystal momentum of the laser-driven electron, and $k(0)$ is the initial crystal momentum at time $t = 0$. For the electron pairs with initial crystal momenta $k(0) = \pm k_0$ in CB1, the oscillating electrons are restricted in the region of $k \in [\pm k_0 - A_0, \pm k_0 + A_0]$, as indicated by the pink-filled zones in Fig. 4(a), where A_0 is the amplitude of the vector potential. Thus the instantaneous band gap between CB1 and the VB reaches the maximum when $k = \pm k_0 \pm A_0$, as indicated by the solid yellow arrows in Fig. 4(a). Considering the symmetry of the energy band, i.e., $E(k_0 + A_0) = E(-k_0 - A_0)$, the maximal instantaneous band gaps are the

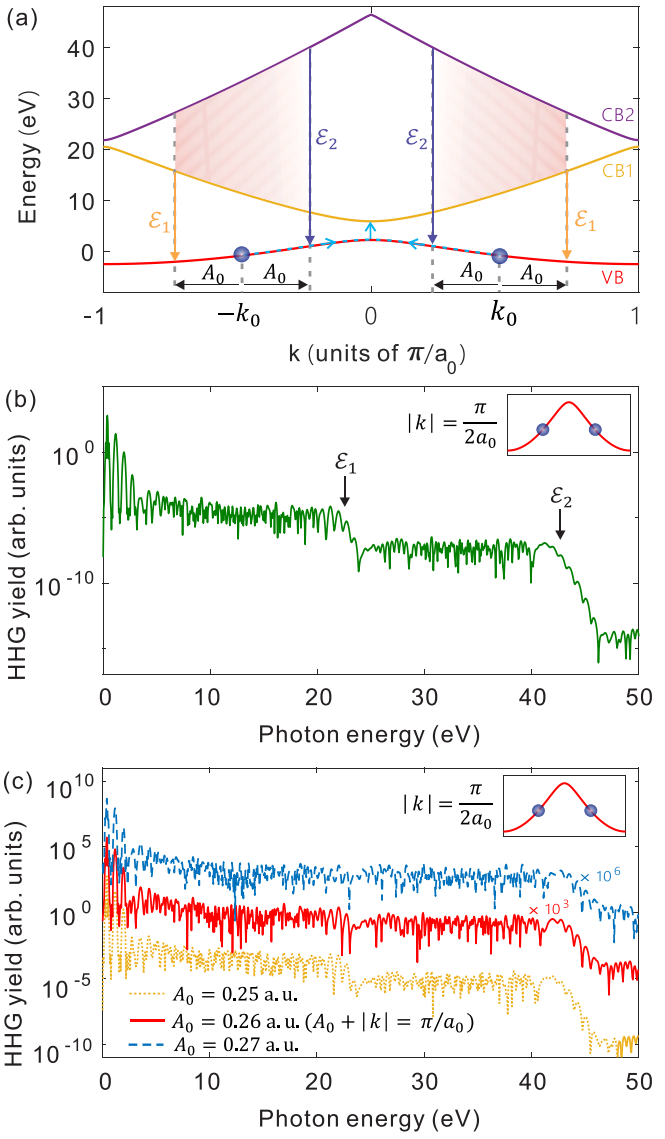

FIG. 4. (a) k-space semiclassical picture for the electron pair with arbitrary crystal momenta $|k_0|$. (b) Harmonic spectrum contributed by the electron pair with $|k| = \pi/(2a_0)$. (c) Harmonic spectra from the electron pair with $|k| = \pi/(2a_0)$ for the vector potentials $A_0 = 0.25$ a.u., 0.26 a.u., and 0.27 a.u. The relation of $A_0 + |k| = \pi/a_0$ exactly holds for $A_0 = 0.26$ a.u. in plane (c).

same for electrons with $+k_0$ and $-k_0$. Therefore the cutoff energy of the first plateau contributed by the electron pair with $|k_0|$ is determined by

$$\mathcal{E}_1 = E_{\mathrm{CB1}}(k_0 + A_0) - E_{\mathrm{VB}}(k_0 + A_0), \tag{14}$$

where E_{CB1} and E_{VB} are the band dispersion relations of CB1 and VB, respectively. Similarly, the instantaneous band gap between CB2 and VB reaches the maximum when $k = \pm k_0 \mp A_0$, as indicated by the solid purple arrows in Fig. 4(a). Thus the cutoff energy of the second plateau contributed by the electron pair with $|k_0|$ is calculated as

$$\mathcal{E}_2 = E_{\mathrm{CB2}}(k_0 - A_0) - E_{\mathrm{VB}}(k_0 - A_0), \tag{15}$$

where E_{CB2} is the band dispersion relation of CB2.

We take the valence electron pair with $|k| = \pi/(2a_0)$ as an example to verify the above-mentioned semiclassical picture. Figure 4(b) shows the calculated harmonic spectrum contributed by the electron pair with $|k| = \pi/(2a_0)$. One can see clearly that two plateaus are evident, as presented in Fig. 4(b). The cutoff energies of the first and second plateaus calculated by Eqs. (14) and (15) are $\mathcal{E}_1 = 22.48$ eV and $\mathcal{E}_2 = 43.01$ eV, respectively. In Fig. 4(b), $\mathcal{E}_1$ and $\mathcal{E}_2$ are indicated by the solid black arrows. It can be seen clearly that the positions of $\mathcal{E}_1$ and $\mathcal{E}_2$ agree very well with the cutoff energies of the first and second plateaus, respectively. It is worth noting that the intensities of the first and second plateaus are nearly the same when the oscillating electron can exceed the Bragg plane, i.e., $|k| + A_0 > \pi/a_0$. At this moment, the first and second plateaus merge with each other. Figure 4(c) shows the harmonic spectra with $A_0 = 0.25$ a.u., 0.26 a.u., and 0.27 a.u. for the electron pair with $|k| = \pi/(2a_0)$. Herein, $A_0 = 0.26$ a.u. exactly satisfies $A_0 + |k| = \pi/a_0$. One can see clearly that the differences of harmonic intensities between the first and second plateaus gradually disappear when $A_0 + |k|$ progressively exceeds π/a_0. The merging of these two plateaus is attributed to the fact that the oscillating electrons in CB1 can reach the Bragg planes and tunnel into CB2 at the positions when $|k| + A_0 > \pi/a_0$. At the band edges, the band gaps between CB2 and CB1 are the global minimum. Thus the second harmonic plateau is significantly enhanced because of the high tunneling probability.

The observed overall harmonic signals are contributed by the coherent summation of currents induced by all independent valence electrons within the whole BZ. The collective dynamics of all individual electrons described by the k-space semiclassical picture result in the observed overall harmonic radiations. Thus the interferences among multiple valence electrons with various crystal momenta should have an important influence on the harmonic plateaus and corresponding cutoff energies. By expanding the considered crystal momentum interval asymptotically, we confirm that each harmonic plateau in the observed overall harmonic spectrum is mainly contributed by the valence electrons located at different crystal momentum zones. Specifically, the valence electrons close to the Γ point ($|k|$ is relatively little) dominate the primary plateaus in the overall harmonic spectra, whereas the valence electrons far away from the Γ point ($|k|$ is relatively great) dominate the latter plateaus in the overall harmonic spectra.

For the sake of discussion, the crystal momenta of all electrons in the VB are sectionalized as shown in Fig. 5(a). Herein, Ω_1, Ω_2, and Ω_3 represent the crystal momentum intervals of $[-\pi/(4a_0), \pi/(4a_0)]$, $[-\pi/(2a_0), \pi/(2a_0)]$, and $[-3\pi/(4a_0), 3\pi/(4a_0)]$, respectively. Figure 5(b) shows calculated harmonic spectra contributed by the electrons at/within the Γ point, Ω_1, Ω_2, and Ω_3. Meanwhile, the observed overall harmonic spectrum is calculated by considering all electrons within the whole BZ and is presented in Fig. 5(b) using the red-filled image. The laser intensity is 4×10^{11} W/cm^2. In Fig. 5(b) one can see that the harmonic plateau from the electron at only the Γ point significantly differs from that of the overall harmonic spectrum. When the electrons within $\Omega_1 = [-\pi/(4a_0), \pi/(4a_0)]$ are considered, the first harmonic plateau is close to that of the overall

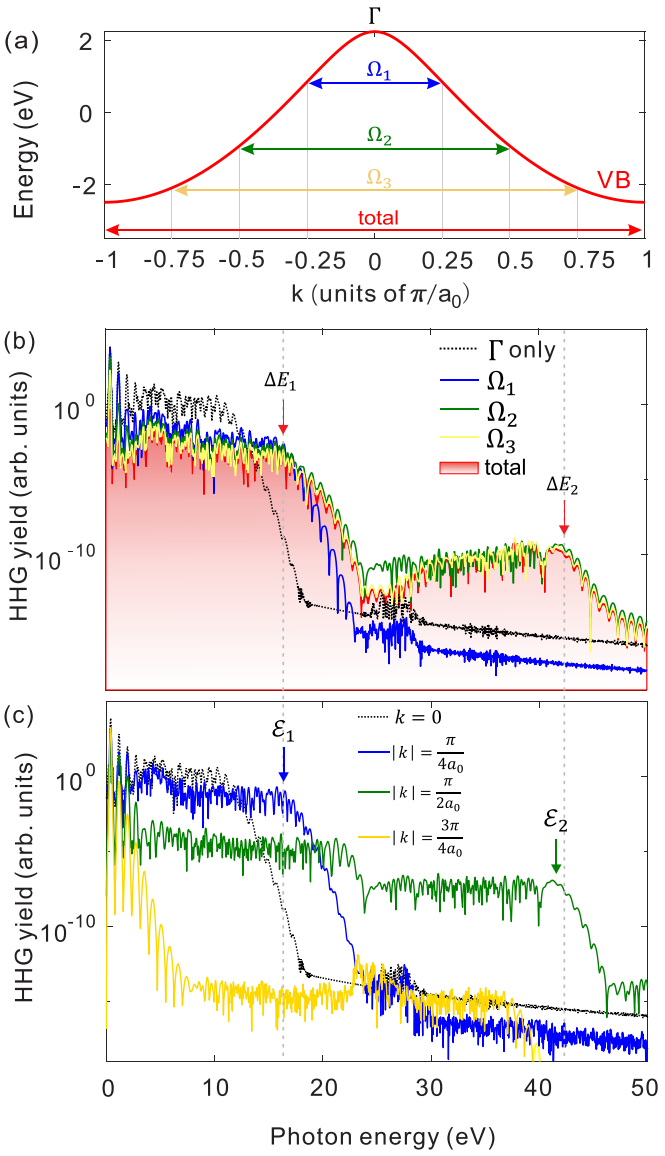

FIG. 5. (a) The sectionalization of crystal momenta for the electrons in VB. Ω_1, Ω_2, and Ω_3 correspond to the crystal momentum intervals of $[-\pi/(4a_0), \pi/(4a_0)]$, $[-\pi/(2a_0), \pi/(2a_0)]$, and $[-3\pi/(4a_0), 3\pi/(4a_0)]$, respectively. (b) Harmonic spectra contributed by the electrons at or within only Γ point, Ω_1, Ω_2, Ω_3 and the whole BZ. (c) Harmonic spectra from a single electron at Γ point and the electron pairs with $|k| = \pi/(4a_0)$, $\pi/(2a_0)$, and $3\pi/(4a_0)$. The laser intensity is 4×10^{11} W/cm^2 in panels (b) and (c).

harmonic spectrum. Herein, the intensities of second harmonic plateaus from the electrons at/within the Γ point and Ω_1 are too low to be seen in Fig. 5(b). When the crystal momentum interval is further expanded as $\Omega_2 = [-\pi/(2a_0), \pi/(2a_0)]$, it is seen that the second plateau of the harmonic spectrum from Ω_2 emerges and is very close to that of the overall harmonic spectrum. Compared with the case of electrons within Ω_1, the first plateau from electrons within Ω_2 is closer to that of the overall harmonic spectrum. The two harmonic plateaus from the electrons within $\Omega_3 = [-3\pi/(4a_0), 3\pi/(4a_0)]$ are almost exactly the same with the overall harmonic spectrum. These results suggest

that the first and second plateaus of the overall harmonic spectrum are mainly contributed by the electron pairs with $|k| \in [0, \pi/(4a_0)]$ and $|k| \in [\pi/(4a_0), \pi/(2a_0)]$, respectively. The valence electrons with $|k| \in [\pi/(2a_0), \pi/a_0]$ only have a minor effect on the overall harmonic spectrum. It should be noted that the sectionalization of crystal momenta for the valence electrons shown in Fig. 5(a) is just a chosen example. The sectionalization is not necessarily strict in our discussion.

We investigate the cutoff energies of harmonic spectra generated by the electron pair with the given $|k|$ to further verify our conclusions. Figure 5(c) shows the harmonic spectra contributed by a single electron at the Γ point and the electron pairs with $|k| = \pi/(4a_0)$, $\pi/(2a_0)$ and $3\pi/(4a_0)$. In Figs. 5(b) and 5(c), the cutoff energies of the first plateau for the harmonic spectrum from the electrons within/at whole BZ and $|k| = \pi/(4a_0)$ are indicated by ΔE_1 and $\mathcal{E}_1$, respectively. The corresponding cutoff energies of the second plateau are indicated by ΔE_2 and $\mathcal{E}_2$. Considering that the first plateau of the overall harmonic spectrum is mainly contributed by the electron pairs with $|k| \in [0, \pi/(4a_0)]$, $\mathcal{E}_1$ and ΔE_1 should be approximately equal. From Figs. 5(b) and 5(c), one can see clearly that $\mathcal{E}_1$ and ΔE_1 are in good agreement with each other as guided by the vertical gray dashed line. Similarly, $\mathcal{E}_2$ should be very close to ΔE_2, which is also validated in Figs. 5(b) and 5(c). The accordance between ΔE_1 and $\mathcal{E}_1$ (or ΔE_2 and $\mathcal{E}_2$) verifies the fact that the multiple plateaus and corresponding cutoff energies of the observed overall harmonic spectra stem from the contributions of valence electrons located at different crystal momentum zones.

We also choose an example with other laser intensities to demonstrate the interference effects among various valence electrons on overall harmonic plateaus. Figure 6(a) shows calculated harmonic spectra contributed by the electron at/within the Γ point, Ω_1, Ω_2, Ω_3, and whole BZ. The laser intensity is 6×10^{11} W/cm^2. One can see clearly that, as the chosen crystal momentum interval is gradually expanded, the obtained first harmonic plateau begins to agree with the first plateau of the overall harmonic spectrum when Ω_1 is considered. Similarly, the obtained second harmonic plateau begins to agree with the second plateau of the overall harmonic spectrum when Ω_2 is considered. Figure 6(b) shows the harmonic spectra contributed by a single electron at the Γ point and the electron pairs with $|k| = \pi/(4a_0)$, $\pi/(2a_0)$ and $3\pi/(4a_0)$. It is noted that the first and second plateaus completely merge for the harmonic spectra from the electron pairs with $\pi/(2a_0)$ and $3\pi/(4a_0)$ because $|k| + A_0 > \pi/a_0$, as illuminated in Fig. 4(c). Similar to the results shown in Figs. 5(b) and 5(c), $\mathcal{E}_1$ and $\mathcal{E}_2$ are respectively close to ΔE_1 and ΔE_2, as indicated by vertical gray dashed lines in Figs. 6(a) and 6(b). These results further confirm the fact that each plateau in the overall multiple-plateau harmonic spectrum cannot be recognized as the contribution only from the individual valence electron (or electron pair). The observed plateaus in the overall harmonic spectra are the consequences of collective responses involving multiple valence electrons with various crystal momenta. Each plateau of the overall harmonic spectrum is identified to be contributed by the valence electrons within the specific crystal momentum zones. We notice that the effects of multiple valence electrons on the harmonic plateaus are also discussed in a recent work in Ref. [40].

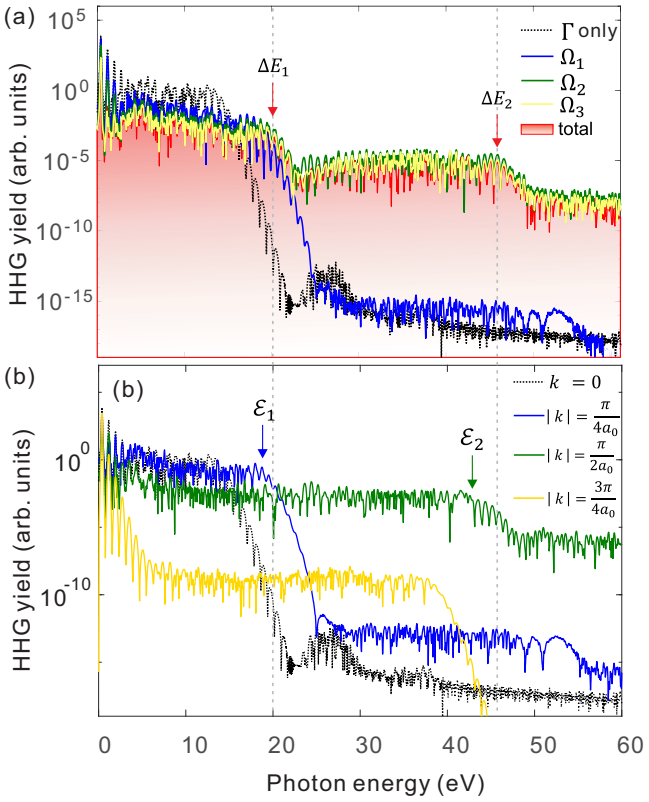

FIG. 6. (a) Harmonic spectra contributed by the electrons at or within only the Γ point, Ω_1, Ω_2, Ω_3 and the whole BZ. (b) Harmonic spectra from a single electron at Γ point and the electron pairs with $|k| = \pi/(4a_0)$, $\pi/(2a_0)$, and $3\pi/(4a_0)$. The laser intensity is 6×10^{11} W/cm^2.

V. BELOW-BAND-GAP HARMONICS

Many studies [31–36,61] suggest that the first plateau of the harmonic spectrum starts from the minimum band gap between the first conduction band and valence band when a solid is irradiated by an intense mid-infrared laser pulse. The harmonics below the minimum band gap are mainly contributed by intraband currents induced by the Bloch oscillations in conduction bands, whereas the harmonics above the minimum band gap are mainly contributed by interband transitions between conduction bands and valence bands. The effects of quantum interferences among valence electrons with various crystal momenta on the below-band-gap harmonics are investigated in this work. Our results show that the contributions from multiple valence electrons result in the significant decreases of harmonic yields in below-band-gap regions for the observed overall harmonics. The remarkable suppression of below-band-gap harmonics originates from the collective dynamics of multiple valence electrons with various crystal momenta and thus cannot be interpreted by the Γ-point-only SAE model.

The harmonic spectrum contributed by all valence electrons within the whole BZ is shown in Fig. 7(a) with a red-filled image. The position of the minimum band gap between CB1 and the VB is indicated by the vertical gray dashed line. In Fig. 7(a), as shown in the laurel-green-shaded area, one can see clearly that the observed overall harmonic spectrum presents an evident dip in the below-band-gap region.

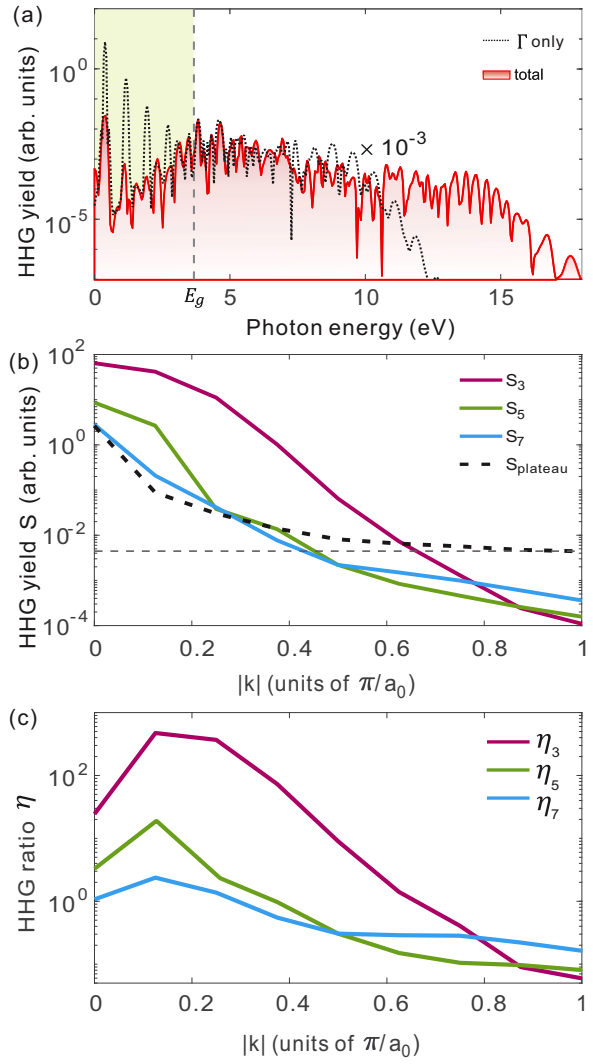

FIG. 7. (a) Harmonic spectra contributed by valence electrons at or within the only Γ point and the whole BZ. (b) Harmonic yield S as the function of $|k|$ for third, fifth, seventh, and the first plateau harmonics. (c) Harmonic intensity ratio η as the function of $|k|$ for the third-, fifth-, and seventh-order harmonics. η represents the intensity ratio between nth-order harmonic and the first harmonic plateau. In plane (a), the vertical gray dashed line indicates the positions of minimum band gap between CB1 and VB, i.e., E_g. In plane (b), the horizontal gray dashed line indicates the value of S_{plateau} when $|k| = 1$.

The yields of below-band-gap harmonics are about one or two orders of magnitude lower than those of the first plateau harmonics. The harmonic spectrum contributed by a single electron at the Γ point is also presented in Fig. 7(a). The subsidence of yields in the below-band-gap harmonic region cannot be observed in the Γ-point-only SAE model. Hence, the vanishing of below-band-gap harmonics in yields is not caused by an individual electron with a specific crystal momentum. The significant suppression of overall below-band-gap harmonics stems from the coherences among multiple valence electrons with different crystal momenta.

In order to explain the suppression effects, we further quantificationally investigate the yields of below-band-gap harmonics by expanding the crystal momentum interval gradually. For a given $|k|$, the intensity of the nth-order harmonic contributed by the valence electrons within crystal momentum interval $[-|k|, |k|]$ is denoted as $S_n(|k|)$. Similarly, the intensity of the first harmonic plateau is denoted as $S_{\text{plateau}}(|k|)$. $S_{\text{plateau}}(|k|)$ is calculated by integrating the harmonic spectrum from 4 to 9 eV. The third-, fifth-, and seventh-order harmonics are considered because only these three order harmonics are located at the below-band-gap region, except for the fundamental frequency field as shown in Fig. 7(a). Figure 7(b) shows the calculated S_n ($n = 3, 5, 7$) and S_{plateau} as a function of $|k|$. One can clearly see that both of S_n and the S_{plateau} decrease monotonically with increasing $|k|$. However, there are some subtle differences between the tendencies of S_n and S_{plateau}. Specifically, S_n descends rapidly with increasing $|k|$ in the whole BZ. S_{plateau} first decreases rapidly when $|k|$ is relatively little, then remains nearly constant when $|k|$ is great enough, as indicated by the horizontal dashed asymptotic line in Fig. 7(b). The different tendencies of S_n and S_{plateau} suggest that the below-band-gap harmonics in the overall harmonic spectra are contributed by all valence electrons within the whole BZ, whereas the first plateau harmonics in the overall harmonic spectra are mainly contributed by only the valence electrons close to the Γ point. In fact, the latter opinion has been verified in Sec. IV. The nearly negligible contributions of the valence electrons far away from the Γ point to the first plateau harmonics in the overall harmonic spectra result in the slow decay of S_{plateau} when all valence electrons are considered. Hence, compared with the slow decay of S_{plateau}, the rapid drop of S_n results in the low relative yields of below-band-gap harmonics. The relative yield of the below-band-gap harmonic is calculated by the intensity ratio between $S_n(|k|)$ and $S_{\text{plateau}}(|k|)$ as

$$\eta_n(|k|) = \frac{S_n(|k|)}{S_{\text{plateau}}(|k|)}. \tag{16}$$

Figure 7(c) shows the calculated harmonic intensity ratio η_n as a function of $|k|$ for third-, fifth-, and seventh-order harmonics. One can see that η_n increases firstly, reaches the maximum at about $|k| = 0.1\pi/a_0$, and rapidly decreases with the further increasing of $|k|$ for these three-order harmonics. From a global perspective, η_n exhibits a distinct descending trend when $|k|$ increases. Eventually, η_n reaches the minimum when all valence electrons are considered, i.e., $|k| = \pi/a_0$. Our results suggest that the interferences among multiple valence electrons with different crystal momenta significantly suppress the generation of below-band-gap harmonics in the overall harmonic spectra.

VI. CONCLUSION

In summary, the interference effects of multiple valence electrons on solid-phase HHG are studied for a band-gap semiconductor in a LP laser pulse. By solving TDSE for the electrons with various crystal momenta, we demonstrate the fact that the dynamics of multiple independent electrons in valence bands result in some unique radiation characteristics of observed harmonic spectra in solids. Our results suggest that the disappearances of even-order harmonics in overall harmonic spectra are the consequences of destructive interferences between the electron pairs with opposite crystal momenta in sign for a crystal with inversion symmetry. It

turns out that each plateau in the overall multiple-plateau harmonic spectrum is mainly contributed by the valence electrons located at different crystal momentum regions. The higher harmonic plateaus are dominated by the valence electrons farther away from the Γ point. The significant suppression of the harmonic yields in the below-band-gap region is observed and is further explained by the interferences among multiple valence electrons. Our work is helpful to gain insight into the ultrafast electron-hole dynamics of multiple valence electrons in solids.

ACKNOWLEDGMENTS

This work was supported by the National Natural Science Foundation of China under Grants No. 12004325, No. 11947042, No. 11904269, No. 11774109, and No. 12021004. This work was also supported by the National Key Research and Development Program of China under Grant No. 2019YFA0308300 and the State Key Laboratory Open Fund of Millimeter Waves under Grant No. K202105. Dongdong Liu is supported by the Jiangsu Qinglan project.

[1] P. B. Corkum, Plasma Perspective on Strong Field Multiphoton Ionization, Phys. Rev. Lett. **71**, 1994 (1993).

[2] F. Krausz and M. Ivanov, Attosecond physics, Rev. Mod. Phys. **81**, 163 (2009).

[3] P. Lan, M. Ruhmann, L. He, C. Zhai, F. Wang, X. Zhu, Q. Zhang, Y. Zhou, M. Li, M. Lein, and P. Lu, Attosecond Probing of Nuclear Dynamics with Trajectory-Resolved High-Harmonic Spectroscopy, Phys. Rev. Lett. **119**, 033201 (2017).

[4] L. He, P. Lan, A.-T. Le, B. Wang, B. Wang, X. Zhu, P. Lu, and C. D. Lin, Real-Time Observation of Molecular Spinning with Angular High-Harmonic Spectroscopy, Phys. Rev. Lett. **121**, 163201 (2018).

[5] Y. Li, T. Sato, and K. L. Ishikawa, High-order harmonic generation enhanced by laser-induced electron recollision, Phys. Rev. A **99**, 043401 (2019).

[6] M. Hentschel, R. Kienberger, C. Spielmann, G. A. Reider, N. Milosevic, T. Brabec, P. Corkum, U. Heinzmann, M. Drescher, and F. Krausz, Attosecond metrology, Nature (London) **414**, 509 (2001).

[7] X. Zhang, X. Zhu, X. Liu, F. Wang, M. Qin, Q. Liao, and P. Lu, Elliptical isolated attosecond-pulse generation from an atom in a linear laser field, Phys. Rev. A **102**, 033103 (2020).

[8] S. Ghimire, A. D. DiChiara, E. Sistrunk, P. Agostini, L. F. DiMauro, and D. A. Reis, Observation of high-order harmonic generation in a bulk crystal, Nat. Phys. **7**, 138 (2011).

[9] Y. S. You, D. A. Reis, and S. Ghimire, Anisotropic high-harmonic generation in bulk crystals, Nat. Phys. **13**, 345 (2017).

[10] T. T. Luu, M. Garg, S. Y. Kruchinin, A. Moulet, M. T. Hassan, and E. Goulielmakis, Extreme ultraviolet high-harmonic spectroscopy of solids, Nature (London) **521**, 498 (2015).

[11] G. Vampa, T. J. Hammond, N. Thiré, B. E. Schmidt, F. Légaré, C. R. McDonald, T. Brabec, D. D. Klug, and P. B. Corkum, All-Optical Reconstruction of Crystal Band Structure, Phys. Rev. Lett. **115**, 193603 (2015).

[12] L. Li, P. Lan, L. He, W. Cao, Q. Zhang, and P. Lu, Determination of Electron Band Structure using Temporal Interferometry, Phys. Rev. Lett. **124**, 157403 (2020).

[13] T. T. Luu and H. J. Wörner, Observing broken inversion symmetry in solids using two-color high-order harmonic spectroscopy, Phys. Rev. A **98**, 041802(R) (2018).

[14] N. Saito, P. Xia, F. Lu, T. Kanai, J. Itatani, and N. Ishii, Observation of selection rules for circularly polarized fields in high-harmonic generation from a crystalline solid, Optica **4**, 1333 (2017).

[15] L. Jia, Z. Zhang, D. Z. Yang, Y. Liu, M. S. Si, G. P. Zhang, and Y. S. Liu, Optical high-order harmonic generation as a structural characterization tool, Phys. Rev. B **101**, 144304 (2020).

[16] K. Kaneshima, Y. Shinohara, K. Takeuchi, N. Ishii, K. Imasaka, T. Kaji, S. Ashihara, K. L. Ishikawa, and J. Itatani, Polarization-Resolved Study of High Harmonics from Bulk Semiconductors, Phys. Rev. Lett. **120**, 243903 (2018).

[17] T. T. Luu and H. J. Wörner, Measurement of the Berry curvature of solids using high-harmonic spectroscopy, Nat. Commun. **9**, 916 (2018).

[18] H. Liu, Y. Li, Y. S. You, S. Ghimire, T. F. Heinz, and D. A. Reis, High-harmonic generation from an atomically thin semiconductor, Nat. Phys. **13**, 262 (2017).

[19] D. Bauer and K. K. Hansen, High-Harmonic Generation in Solids with and without Topological Edge States, Phys. Rev. Lett. **120**, 177401 (2018).

[20] R. E. F. Silva, Á. Jiménez-Galán, B. Amorim, O. Smirnova, and M. Ivanov, Topological strong-field physics on sub-laser-cycle timescale, Nat. Photon. **13**, 849 (2019).

[21] A. Chacón, W. Zhu, S. P. Kelly, A. Dauphin, E. Pisanty, A. Picón, C. Ticknor, M. F. Ciappina, A. Saxena, and M. Lewenstein, Observing topological phase transitions with high harmonic generation, Phys. Rev. B **102**, 134115 (2020).

[22] G. Vampa, T. J. Hammond, M. Taucer, X. Ding, X. Ropagnol, T. Ozaki, S. Delprat, M. Chaker, N. Thiré, B. E. Schmidt, F. Légaré, D. D. Klug, A. Y. Naumov, D. M. Villeneuve, A. Staudte, and P. B. Corkum, Strong-field optoelectronics in solids, Nat. Photon. **12**, 465 (2018).

[23] C. Yu, K. K. Hansen, and L. B. Madsen, Enhanced high-order harmonic generation in donor-doped band-gap materials, Phys. Rev. A **99**, 013435 (2019).

[24] X. Liu, L. Li, X. Zhu, T. Huang, X. Zhang, D. Wang, P. Lan, and P. Lu, Wavelength dependence of high-order harmonic yields in solids, Phys. Rev. A **98**, 063419 (2018).

[25] S. Fu, Y. Feng, J. Li, S. Yue, X. Zhang, B. Hu, and H. Du, Recollision dynamics analysis of high-order harmonic generation in solids, Phys. Rev. A **101**, 023402 (2020).

[26] A. J. Uzan, G. Orenstein, Á. Jiménez-Galán, C. McDonald, R. E. F. Silva, B. D. Bruner, N. D. Klimkin, V. Blanchet, T. Arusi-Parpar, M. Krüger, A. N. Rubtsov, O. Smirnova, M. Ivanov, B. Yan, T. Brabec, and N. Dudovich, Attosecond spectral singularities in solid-state high-harmonic generation, Nat. Photon. **14**, 183 (2020).

[27] S. Ghimire, G. Ndabashimiye, A. D. DiChiara, E. Sistrunk, M. I. Stockman, P. Agostini, L. F. DiMauro, and D. A. Reis,

Strong-field and attosecond physics in solids, J. Phys. B: At. Mol. Opt. Phys. **47**, 204030 (2014).
[28] S. Y. Kruchinin, F. Krausz, and V. S. Yakovlev, Colloquium: Strong-field phenomena in periodic systems, Rev. Mod. Phys. **90**, 021002 (2018).
[29] G. Vampa and T. Brabec, Merge of high harmonic generation from gases and solids and its implications for attosecond science, J. Phys. B: At. Mol. Opt. Phys. **50**, 083001 (2017).
[30] S. Ghimire and D. A. Reis, High-harmonic generation from solids, Nat. Phys. **15**, 10 (2019).
[31] M. Wu, D. A. Browne, K. J. Schafer, and M. B. Gaarde, Multilevel perspective on high-order harmonic generation in solids, Phys. Rev. A **94**, 063403 (2016).
[32] X. Liu, X. Zhu, P. Lan, X. Zhang, D. Wang, Q. Zhang, and P. Lu, Time-dependent population imaging for high-order-harmonic generation in solids, Phys. Rev. A **95**, 063419 (2017).
[33] G. Ndabashimiye, S. Ghimire, M. Wu, D. A. Browne, K. J. Schafer, M. B. Gaarde, and D. A. Reis, Solid-state harmonics beyond the atomic limit, Nature (London) **534**, 520 (2016).
[34] G. Vampa, C. R. McDonald, G. Orlando, D. D. Klug, P. B. Corkum, and T. Brabec, Theoretical Analysis of High-Harmonic Generation in Solids, Phys. Rev. Lett. **113**, 073901 (2014).
[35] X. Liu, X. Zhu, X. Zhang, D. Wang, P. Lan, and P. Lu, Wavelength scaling of the cutoff energy in the solid high harmonic generation, Opt. Express **25**, 29216 (2017).
[36] M. Wu, S. Ghimire, D. A. Reis, K. J. Schafer, and M. B. Gaarde, High-harmonic generation from Bloch electrons in solids, Phys. Rev. A **91**, 043839 (2015).
[37] J. Luo and F. Chen, High harmonic generation from a two-dimensional square lattice by a circularly polarized laser pulse, J. Opt. Soc. Am. B **35**, 3104 (2018).
[38] J.-B. Li, X. Zhang, S.-J. Yue, H.-M. Wu, B.-T. Hu, and H.-C. Du, Enhancement of the second plateau in solid high-order harmonic spectra by the two-color fields, Opt. Express **25**, 18603 (2017).
[39] T.-Y. Du and X.-B. Bian, Quasi-classical analysis of the dynamics of the high-order harmonic generation from solids, Opt. Express **25**, 151 (2017).
[40] C. Yu, H. Iravani, and L. B. Madsen, Crystal-momentum-resolved contributions to multiple plateaus of high-order harmonic generation from band-gap materials, Phys. Rev. A **102**, 033105 (2020).
[41] J. Li, S. Fu, H. Wang, X. Zhang, B. Ding, B. Hu, and H. Du, Limitations of the single-active-electron approximation in quantum simulations of solid high-order harmonic generation, Phys. Rev. A **98**, 043409 (2018).
[42] L.-J. Lü and X.-B. Bian, Multielectron interference of intraband harmonics in solids, Phys. Rev. B **100**, 214312 (2019).
[43] L. Li, P. Lan, X. Zhu, T. Huang, Q. Zhang, M. Lein, and P. Lu, Reciprocal-Space-Trajectory Perspective on High-Harmonic Generation in Solids, Phys. Rev. Lett. **122**, 193901 (2019).
[44] T. Ikemachi, Y. Shinohara, T. Sato, J. Yumoto, M. Kuwata-Gonokami, and K. L. Ishikawa, Trajectory analysis of high-order-harmonic generation from periodic crystals, Phys. Rev. A **95**, 043416 (2017).
[45] F. Navarrete, M. F. Ciappina, and U. Thumm, Crystal-momentum-resolved contributions to high-order harmonic generation in solids, Phys. Rev. A **100**, 033405 (2019).
[46] G.-R. Jia, X.-Q. Wang, T.-Y. Du, X.-H. Huang, and X.-B. Bian, High-order harmonic generation from 2D periodic potentials in circularly and bichromatic circularly polarized laser fields, J. Chem. Phys. **149**, 154304 (2018).
[47] J. Crank and P. Nicolson, A practical method for numerical evaluation of solutions of partial differential equations of the heat-conduction type, Adv. Comput. Math. **6**, 207 (1996).
[48] K. K. Hansen, T. Deffge, and D. Bauer, High-order harmonic generation in solid slabs beyond the single-active-electron approximation, Phys. Rev. A **96**, 053418 (2017).
[49] N. Tancogne-Dejean, O. D. Mücke, F. X. Kärtner, and A. Rubio, Impact of the Electronic Band Structure in High-Harmonic Generation Spectra of Solids, Phys. Rev. Lett. **118**, 087403 (2017).
[50] I. Floss, C. Lemell, G. Wachter, V. Smejkal, S. A. Sato, X.-M. Tong, K. Yabana, and J. Burgdörfer, Ab initio multiscale simulation of high-order harmonic generation in solids, Phys. Rev. A **97**, 011401(R) (2018).
[51] O. E. Alon, V. Averbukh, and N. Moiseyev, Selection Rules for the High Harmonic Generation Spectra, Phys. Rev. Lett. **80**, 3743 (1998).
[52] F. Ceccherini, D. Bauer, and F. Cornolti, Dynamical symmetries and harmonic generation, J. Phys. B: At. Mol. Opt. Phys. **34**, 5017 (2001).
[53] X. Liu, X. Zhu, L. Li, Y. Li, Q. Zhang, P. Lan, and P. Lu, Selection rules of high-order-harmonic generation: Symmetries of molecules and laser fields, Phys. Rev. A **94**, 033410 (2016).
[54] A. D. Bandrauk, F. Mauger, and K.-J. Yuan, Circularly polarized harmonic generation by intense bicircular laser pulses: Electron recollision dynamics and frequency dependent helicity, J. Phys. B: At. Mol. Opt. Phys. **49**, 23LT01 (2016).
[55] D. M. Reich and L. B. Madsen, Illuminating Molecular Symmetries with Bicircular High-Order-Harmonic Generation, Phys. Rev. Lett. **117**, 133902 (2016).
[56] N. Moiseyev, Selection rules for harmonic generation in solids, Phys. Rev. A **91**, 053811 (2015).
[57] O. Neufeld, D. Podolsky, and O. Cohen, Floquet group theory and its application to selection rules in harmonic generation, Nat. Commun. **10**, 405 (2019).
[58] Y. Sanari, T. Otobe, Y. Kanemitsu, and H. Hirori, Modifying angular and polarization selection rules of high-order harmonics by controlling electron trajectories in k-space, Nat. Commun. **11**, 3069 (2020).
[59] G. Vampa, T. J. Hammond, N. Thiré, B. E. Schmidt, F. Légaré, C. R. McDonald, T. Brabec, and P. B. Corkum, Linking high harmonics from gases and solids, Nature (London) **522**, 462 (2015).
[60] L. Plaja and L. Roso-Franco, High-order harmonic generation in a crystalline solid, Phys. Rev. B **45**, 8334 (1992).
[61] Y.-T. Zhao, S.-C. Jiang, X. Zhao, J.-G. Chen, and Y.-J. Yang, Effect of interband polarization on a solid's high-order-harmonic generation just below the band gap, Opt. Lett. **45**, 2874 (2020).